ACS OMEGA

http://pubs.acs.org/journal/acsodf

Article

Crystal Structures of Fsa2 and Phm7 Catalyzing [4 + 2] Cycloaddition Reactions with Reverse Stereoselectivities in Equisetin and Phomasetin Biosynthesis

Changbiao Chi,[§] Zhengdong Wang,[§] Tan Liu, Zhongyi Zhang, Huan Zhou, Annan Li, Hongwei Jin, Hongli Jia, Fuling Yin, Donghui Yang, and Ming Ma*

Cite This: *ACS Omega* 2021, 6, 12913−12922

Read Online

ACCESS | Metrics & More | Article Recommendations | Supporting Information

ABSTRACT: Fsa2 and Phm7 are a unique pair of pericyclases catalyzing [4 + 2] cycloaddition reactions with reverse stereoselectivities in the biosynthesis of equisetin and phomasetin, both of which are potent HIV-1 integrase inhibitors. We here solve the crystal structures of Fsa2 and Phm7, both of which possess unusual "two-β barrel" folds. Different residues are evident between the active sites of Fsa2 and Phm7, and modeling experiments provide key structural information determining the reverse stereoselectivities. These results provide a better understanding of how natural pericyclases control the catalytic stereoselectivities and benefit the protein engineering in future.

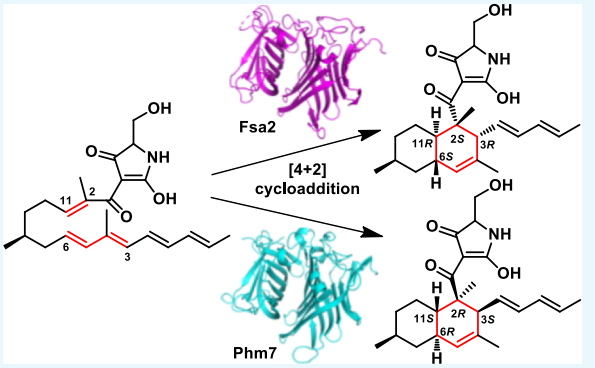

INTRODUCTION

The cycloaddition reactions are powerful carbon−carbon bond-forming reactions in synthetic chemistry. Such reactions are also utilized in natural product biosynthesis, and biosynthetic enzymes catalyzing [4 + 2] or [6 + 4] cycloadditions are receiving increased attention.[1,2] Since the identification of the first standalone [4 + 2] pericyclase SpnF in spinosyns biosynthesis,[3] a series of pericyclases have been discovered in polyketide, alkaloid, terpenoid, and thiopeptide biosynthesis from microorganism and plant origins. These pericyclases construct featured chemical skeletons or key moieties, such as PyrE3 and PyrI4 catalyzing decalin and spirotetramate formations in pyrroindomycin biosynthesis,[4,5] MycB catalyzing decalin formation in myceliothermophin biosynthesis,[6] AbyU/AbmU catalyzing spirotetronate formations in abyssomicin/neoabyssomicin biosynthesis,[7,8] TbtD/TclM/PbtD catalyzing pyridine-like ring formation in thiomuracin GZ/thiocillins/GE2270A biosynthesis,[9−11] StmD catalyzing [6 + 4] cycloaddition to form a 10-membered ring in streptoseomycin biosynthesis,[12] MaDA catalyzing intermolecular [4 + 2] cycloaddition to form a cyclohexane-like ring in chalcomoracin biosynthesis,[13] and LepI/EpiI catalyzing hetero-Diels−Alder reactions to form a pyran-like ring in leporin and fusaricide biosynthesis.[14−16] A summary of these pericyclases' catalysis is depicted in Figure S1, highlighting their diverse and powerful roles in natural product biosynthesis.

The most fascinating feature of these pericyclases is their stereoselectivity in the cycloaddition. From the view of this aspect, one pair of pericyclases Fsa2/Phm7 is unique in all reported pericyclases because they catalyze reversely stereoselective [4 + 2] cycloadditions using similar substrates to generate four pairs of reverse chiral centers.[17,18] Fsa2 and Phm7 are involved in decalin skeleton formation in the biosynthesis of equisetin and its enantiomeric homologue phomasetin (Figure 1A), respectively, both of which are potent HIV-1 integrase inhibitors.[19] Fsa2 generates 2*S*,3*R*,6*S*,11*R* configurations in equisetin and Phm7 generates 2*R*,3*S*,6*R*,11*S* configurations in phomasetin, and the two enzymes' reverse stereoselectivities were further evidenced when Fsa2 reacted with the native substrate of Phm7 (Figure 1B).[18] Until now, the structural basis for their reverse stereoselectivities remains elusive. Other features of the biosynthetic pericyclases can be observed in their low sequence similarities and diverse tertiary structures.[2] Fsa2 and Phm7 share 37% sequence identity to each other but both of them share almost no sequence similarities with all other reported pericyclases (except the just reported CghA). Whether Fsa2 and Phm7 share tertiary structure similarities with others or possess novel structural folds is worthy of investigation. We previously solved the

Received: March 24, 2021
Accepted: April 23, 2021
Published: May 6, 2021

https://doi.org/10.1021/acsomega.1c01593
ACS Omega 2021, 6, 12913−12922

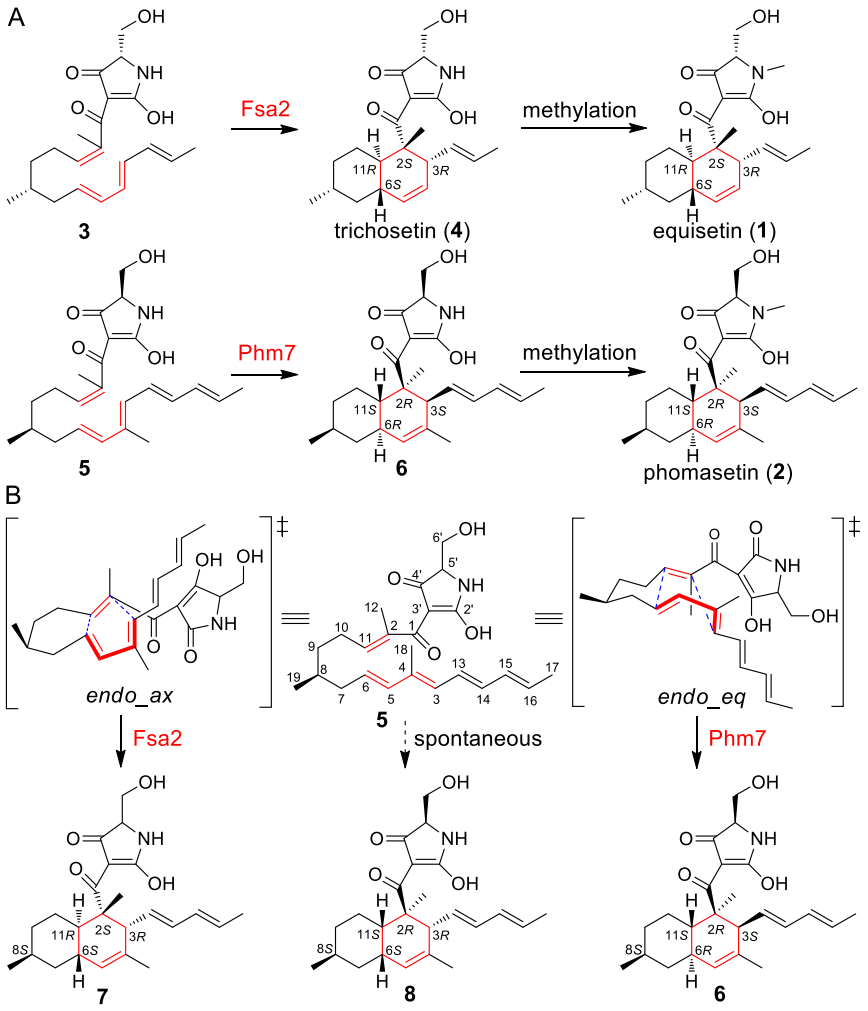

Figure 1. [4 + 2] Cycloaddition reactions catalyzed by Fsa2 and Phm7. (A) Fsa2 and Phm7 catalyze the formations of four pairs of reverse chiral centers at C2/C3/C6/C11 in equisetin and phomasetin biosynthesis, respectively. (B) Reactions catalyzed by Fsa2 and Phm7 with reverse stereoselectivities using the same substrate **5**. The six-membered rings generated by Fsa2 and Phm7 are labeled in red, and the cycloaddition positions are indicated with blue dashed lines.

crystal structure of pericyclase AbmU and provided the structural basis for its stereoselectivity in neoabyssomicin biosynthesis.[8] In this study, we report the crystal structures of Fsa2 and Phm7, which show unusual "two-β barrel" structures and distinct active sites from each other. The reverse stereoselectivites of Fsa2 and Phm7 are elucidated based on their different active sites and docking experiments.

RESULTS AND DISCUSSION

Since the sequences of Fsa2 and Phm7 have been published,[17,18] we directly synthesized the Fsa2- and Phm7-encoded DNAs that were optimized for expression in *Escherichia coli* and inserted them individually into the plasmid pET28b, generating *fsa2*-bearing plasmid pMM4005 and *phm7*-bearing plasmid pMM4006. Transformation of pMM4005 and pMM4006 individually into *E. coli* BL21 (DE3) and gene expression were carried out, leading to the production of Fsa2 and Phm7, which were digested by thrombin to remove the His_6-tag and purified to homogeneity. High-quality crystals of Fsa2 and Phm7 were successfully obtained after multiple rounds of crystallization screening and optimization. The crystal structure of Fsa2 was solved at 2.00 Å by a single-wavelength anomalous diffraction (Se-SAD) method after collecting 3600 X-ray diffraction images at beamline BL17U1 at Shanghai Synchrotron Radiation Facility (SSRF).[20] The crystal structure of Phm7 was solved at 2.00 Å by molecular replacement using the Fsa2 structure as the searching model.

The overall structure of Fsa2 possesses two antiparallel β barrels linked with an α helix (Figure 2A). There is one molecule in one asymmetric unit, and electron density map was well-defined for residues 3−275, 280−292, and 295−377 (residues 1−3 are encoded by the plasmid sequence instead of the *fsa2* sequence). The two β barrels are orthogonally packed with each axis perpendicular to the other (Figure S3A). The N-terminal β barrel of Fsa2 (residues 3−215) comprises 14 β strands (β1−β14) and one α helix (α1 between β3 and β4), and the C-terminal β barrel (residues 224−377) comprises nine β strands (β15−β23). The N- and C-terminal β barrels show structural homology to each other with a root-mean-square deviation (rmsd) of 3.37 Å for 108 Cα atoms (Figure S4A). One α helix (α2) is located between β14 and β15 bridging the two β barrels. A long loop between β1 and β2 covers one side of entrance of the N-terminal β barrel, and this loop interacts with another long loop between β10 and β11 (Figure S3C). The overall structure of Phm7 shows highly

https://doi.org/10.1021/acsomega.1c01593
ACS Omega 2021, 6, 12913−12922

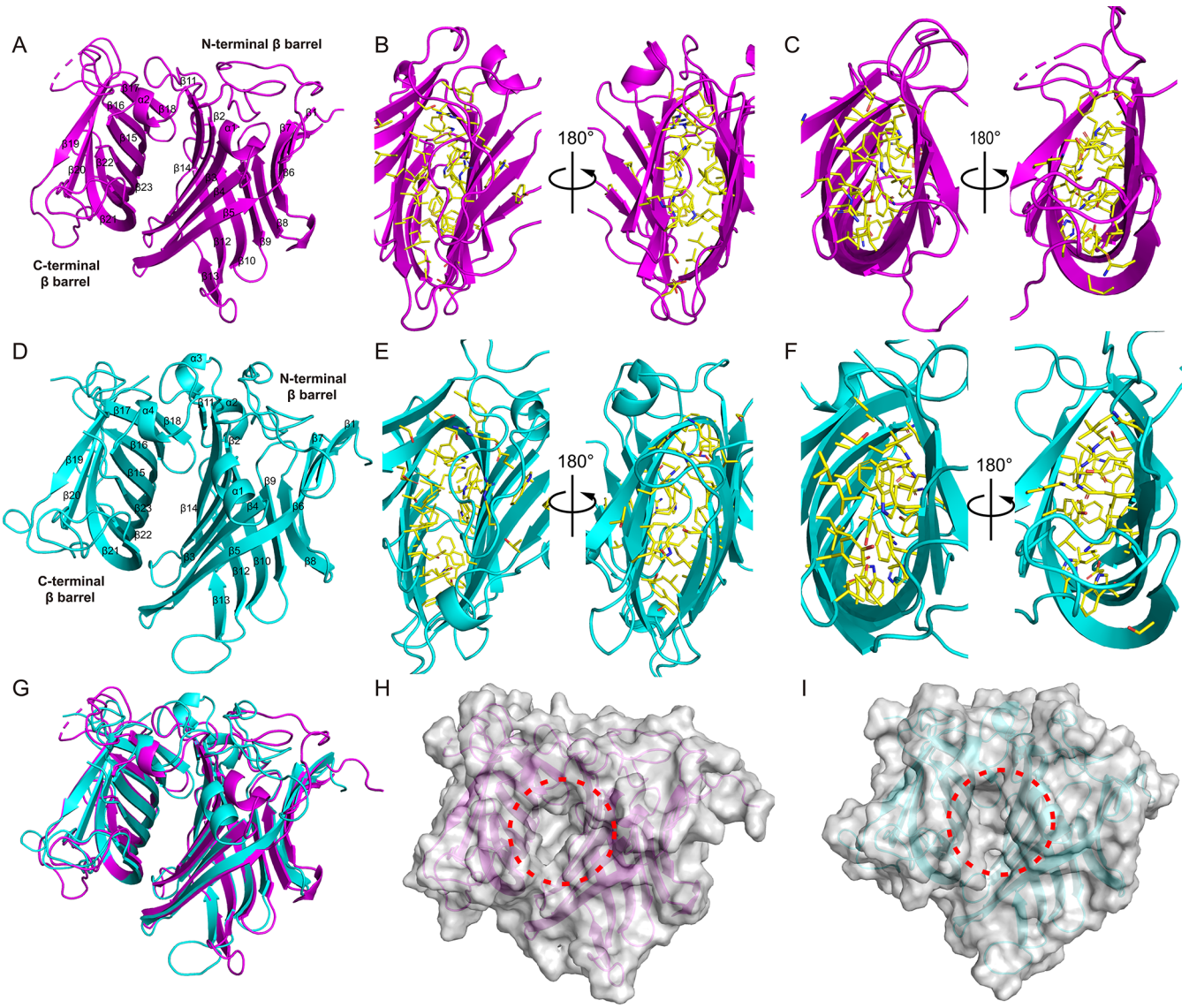

Figure 2. Crystal structures and active sites of Fsa2 and Phm7. (A) "Two-β barrel" structure of Fsa2. (B) View from two entrances of the N-terminal β barrel of Fsa2, which is fully filled with nonpolar residues (labeled in yellow sticks). (C) View from two entrances of the C-terminal β barrel of Fsa2, which is fully filled with nonpolar residues (labeled in yellow sticks). (D) "Two-β barrel" structure of Phm7. (E) View from two entrances of the N-terminal β barrel of Phm7, which is fully filled with nonpolar residues (labeled in yellow sticks). (F) View from two entrances of the C-terminal β barrel of Phm7, which is fully filled with nonpolar residues (labeled in yellow sticks). (G) Superimposition of Fsa2 and Phm7 structures. (H) Surface representation of Fsa2 with the same view direction as that for (A). (I) Surface representation of Phm7 with the same view direction as that for (D). The active sites of Fsa2 and Phm7 are indicated with red dashed circles.

similar "two-β barrel" folds to Fsa2 with an rmsd of 1.32 Å for 334 Cα atoms (Figure 2D,G). There are six molecules in one asymmetric unit, and electron density map was well-defined for residues 5−281 and 293−389 (residues 1−3 are encoded by the plasmid sequence instead of the *phm7* sequence). Superimposition of the six molecules in one asymmetric unit of Phm7 shows that their tertiary structures including residues' side chains are almost the same (Figure S5). The N-terminal β barrel of Phm7 (residues 5−221) comprises 14 β strands (β1−β14) and three α helices (α1 between β3 and β4; α2 and α3 between β10 and β11), and the C-terminal β barrel (residues 231−389) comprises nine β strands (β15−β23). The extension of the C-terminal of β5 and N-terminal of β6 leads to a long β strand in Phm7. Similar to Fsa2, Phm7 possesses one α helix (α4) between β14 and β15 bridging the two β barrels and a long loop between β1 and β2 covering one side of the entrance of the N-terminal β barrel. The long loop also interacts with the loop between β10 and β11, in which region two additional α2 and α3 helices are present compared to that in Fsa2 (Figures S3D and S6). Dali alignment only reveals two homologues with evident similarities to Fsa2 and Phm7: CghA (PDB ID: 6KAW and 6KBC) that is the pericyclase in Sch210972 biosynthesis[21] and NE1406 (PDB ID: 2ICH) whose function is unknown (no evidence indicating that it is a pericyclase) (Figure 3A).[22] The structure of CghA belongs to a parallel research that is just published during this manuscript preparation. By summarizing all published tertiary structures of pericyclases, we can roughly classify them into several groups: one-β barrel structures including PyrI4, AbyU, and AbmU; α + β barrel structures including StmD, NgnD, 101015D, and IdmH; and other structures that show diverse folds including SpnF, PyrE3, PbtD, TbtD, MaDA, PdxI, MalC, and PhqE

https://doi.org/10.1021/acsomega.1c01593
ACS Omega 2021, 6, 12913−12922

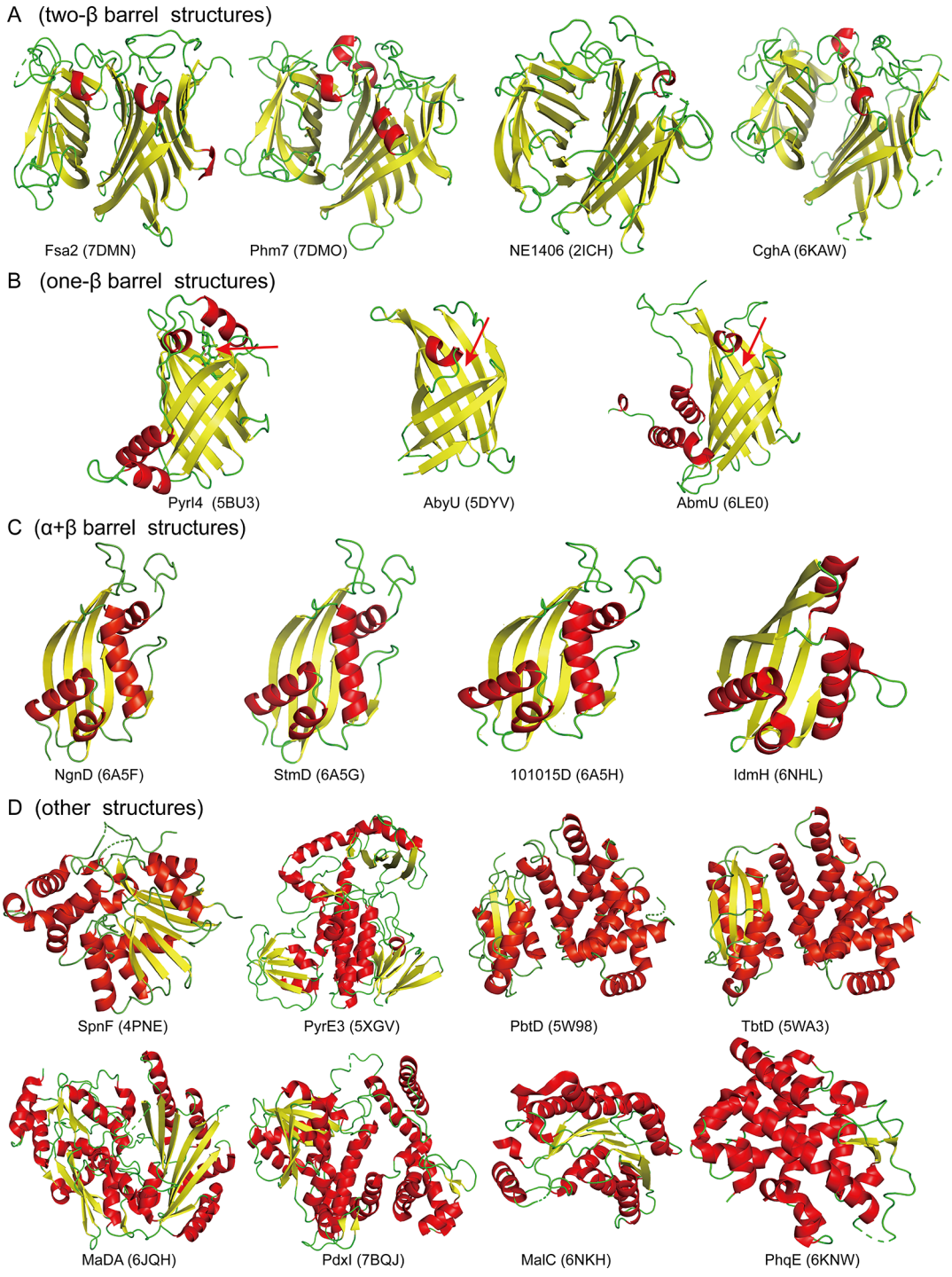

Figure 3. Structural comparison of Fsa2 and Phm7 with other pericyclases. (A−D) Different groups of pericyclases based on their structural folds. The α helices and β strands are shown in red and yellow, respectively. The red arrows in (B) indicate the active sites. PDB IDs are shown in parentheses.

(Figure 3). The two-β barrel structures of Fsa2 and Phm7, together with CghA, are distinct from all published pericyclases, enriching the structural diversity of this important family of enzymes.

The two-β barrel structures of Fsa2 and Phm7 make it interesting to define their catalytic active sites. In one-β barrel structures PyrI4, AbyU, and AbmU, the active sites inside the β barrels have been well-characterized (Figure 3B).[4,7,8] Therefore, we began to check whether there are possible active pockets in the N- and C-terminal β barrels of Fsa2 and Phm7. Unexpectedly, both the N- and C-terminal β barrels of Fsa2 and Phm7 are fully filled with dense hydrophobic interactions from side chains of residues, excluding possible spaces for substrates binding (Figure 2B,C,E,F). The β barrel in PyrI4, AbyU, or AbmU comprises conserved eight β strands, whereas the N- and C-terminal β barrels in Fsa2 or Phm7 comprises 14 and nine β strands, respectively. Compared to the β barrels in PyrI4, AbyU, or AbmU, the N- and C-terminal β barrels in Fsa2 or Phm7 are much more flattened due to the dense hydrophobic interactions inside (Figure S7). These flattened

https://doi.org/10.1021/acsomega.1c01593
ACS Omega 2021, 6, 12913−12922

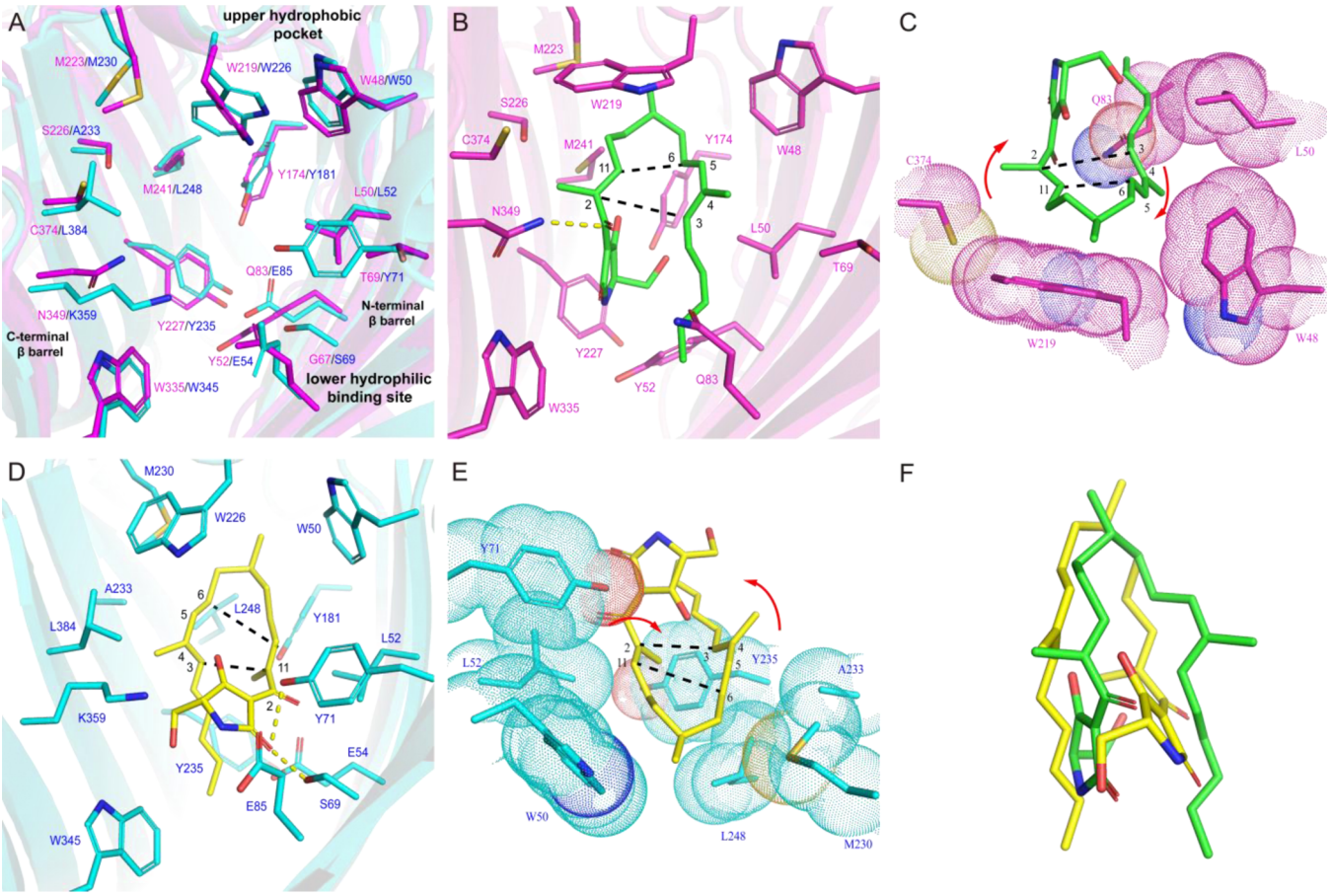

Figure 4. Active sites of Fsa2 and Phm7 and modeling experiments. (A) Comparison between active sites of Fsa2 (magenta) and Phm7 (cyan). (B) Modeling of 5 (green) in the active site of Fsa2. (C) Shape complementarities of diene/dienophile moieties of 5 to the active site of Fsa2. Key residues are shown in dot presentation. (D) Modeling of 5 (yellow) in the active site of Phm7. (E) Shape complementarities of diene/dienophile moieties of 5 to the active site of Phm7. Key residues are shown in dot presentation. (F) Superimposition of modeled 5 (green for Fsa2 and yellow for Phm7) in the active sites of Fsa2 and Phm7. Residues' names are labeled in magenta for Fsa2 and blue for Phm7. The hydrogen bonds are indicated with yellow dashed lines and the cycloaddition positions are indicated with black dashed lines. Red arrows indicate the rotation directions of diene/dienophile moieties during the cycloaddition reactions.

and fully filled N- and C-terminal β barrels imply roles for whole structural stability instead of substrate binding, which is consistent with the observation that Fsa2 could be tolerant to high reaction temperature and organic solvents.[23] We then checked other parts of Fsa2 and Phm7 for locating the possible active sites. After analyzing the surfaces of whole structures of Fsa2 and Phm7, two deep cavities were clearly located at the interfaces between the N- and C-terminal β barrels in Fsa2 and Phm7, respectively (Figure 2H,I). Two glycerol molecules from the cryoprotectant solution are present in the deep cavity of Fsa2, suggesting a possible substrate-binding site (Figure S8). Such an active site at the interface between two β barrels has been proposed for NE1406[22] and further confirmed by the complex structure of CghA with the product Sch210972.[21]

We next compared the two active sites to dig out key structural information determining their reverse catalytic stereoselectivities. Both the active sites of Fsa2 and Phm7 consist of an upper hydrophobic pocket and a lower hydrophilic binding site that contains polar residues (Figure 4A). A conserved tryptophan residue (Trp219 in Fsa2 or Trp226 in Phm7) from the α helix, which bridges the two β barrels, caps the upper hydrophobic pocket in Fsa2 or Phm7. Another conserved tryptophan residue (Trp335 in Fsa2 or Trp345 in Phm7) from the C-terminal β barrel seals the active site in the lower hydrophilic binding site. Besides the capping tryptophan residue, the upper pocket of Fsa2 consists of Cys374, Met223, Met241, and Tyr228 from the C-terminal β barrel, and Tyr174, Trp48, Leu50, and Tyr52 from the N-terminal β barrel; correspondingly, the upper pocket of Phm7 consists of residues at the similar positions including Lue384, Met230, Leu248, and Tyr235 from the C-terminal β barrel, and Tyr181, Trp50, Leu52, and Glu54 from the N-terminal β barrel (Figure 4A). We propose that the upper hydrophobic pocket in Fsa2 or Phm7 is responsible for accommodating the linear diene/dienophile-containing polyketide part of the substrate, and different types and positions of residues in the two upper hydrophobic pockets define different shapes of active sites (Figure 2H,I), contributing to their different catalytic stereoselectivities. The lower hydrophilic binding sites in Fsa2 and Phm7 show different polar residues. In this region, Fsa2 contains Asn349 from the C-terminal β barrel and Thr69 from the N-terminal β barrel, whereas Phm7 contains two corresponding residues Lys359 and Tyr71 at the similar positions but contains one more residue Ser69 (corresponding to Gly67 in Fsa2) from the N-terminal β barrel. The lower hydrophilic binding site is proposed to interact with the polar tetramate moiety of the substrate, and different polar residues

https://doi.org/10.1021/acsomega.1c01593
ACS Omega 2021, 6, 12913−12922

in this region between Fsa2 and Phm7 suggest different binding styles with the substrates' tetramate moiety.

To achieve a better understanding of the catalytic mechanisms of Fsa2 and Phm7, we tried to solve the complex structures of Fsa2 with equisetin by multiple rounds of cocrystallization and soaking, but these experiments failed after great effort was made. The substrate mimics of Fsa2 have been chemically synthesized before;[24] however, given the multiple issues including stereoisomeric side products, difficulties in product purification, and nonenzymatic cycloadditions in the synthesis, we did not synthesize the substrate mimics of Fsa2 or Phm7 for cocrystallization at this time. We then modeled substrate **5**, which can be catalyzed by both Fsa2 and Phm7 to produce **7** and **6**,[18] respectively, into the active sites of Fsa2 and Phm7 (Figure 4B,D). Modeling of **5** into the active site of Fsa2 shows that the linear polyketide part of **5** is curled in the upper hydrophobic pocket, making the $\Delta^{3,4}$ and $\Delta^{5,6}$-diene moiety close to the $\Delta^{2,11}$-dienophile moiety, satisfying the cycloaddition. This curled conformation is achieved by the tight hydrophobic interactions with the nonpolar residues mentioned above in the upper hydrophobic pocket, with Trp219 covering at the top of the diene and dienophile moieties. A hydrogen bond is evident between the lactam carbonyl group and Asn349 from the C-terminal β barrel, stabilizing the tetramate moiety in the lower hydrophilic binding site (Figure 4B). The four possible transition-state structures of the substrate mimics of Fsa2 and Phm7 have been proposed and their activation free energies have been previously calculated by density functional theory calculations.[18] The binding conformation of **5** in the active sites of Fsa2 is consistent with the *endo_ax* structure (Figure 1B).[17,18] Such a binding conformation is a complementarity to the active site shape, in which Trp48 and Leu50 interact with the $\Delta^{3,4}$ and $\Delta^{5,6}$-diene moiety from one side and Cys374 interacts with the $\Delta^{2,11}$-dienophile moiety from the other side to achieve the "correct" stereoselectivity (Figure 4C). Modeling of **5** into the active site of Phm7 shows that the substrate is also curled to satisfy the cycloaddition reaction by tight interactions with nonpolar residues in the upper hydrophobic pocket, but the conformation of the curled **5** is almost rotated by 180° compared to modeled **5** in the active site of Fsa2 (Figure 4B,D,F). The lactam carbonyl group of the tetramate moiety forms hydrogen bonds with Ser69 and Tyr71 from the N-terminal β barrel, suggesting important roles of these polar residues in the substrate binding (Figure 4D). The binding conformation of **5** in the active sites of Phm7 is consistent with the *endo_eq* structure (Figure 1B).[18] Such a binding conformation is a complementarity to the active site shape of Phm7, in which Met230, Ala233, Tyr235, and Leu248 interact with the $\Delta^{3,4}$ and $\Delta^{5,6}$-diene moiety from one side, and Trp50, Leu52, and Tyr71 interact with the $\Delta^{2,11}$-dienophile moiety from the other side, to achieve the reverse stereoselectivity to Fsa2 (Figure 4E). The shape complementary bindings of **5** in Fsa2 and Phm7 support their stereoselective productions of **7** and **6** instead of **8** (Figure 1B), which is a spontaneous product with different cycloaddition stereoselectivities.

Modeling of products **7** into the active site of Fsa2 and **6** into the active site of Phm7 shows that **7** and **6** possess similar binding styles to their corresponding substrates in the two active sites (Figure S9). The C-1 carbonyl group of modeled **7** is toward Ser226 (corresponding to Ala233 in Phm7) in Fsa2. The Ser226 interacts with two water molecules that form hydrogen bonds with two glycerol molecules in Fsa2 structures (Figure S8), thereby it cannot be excluded that Ser226 may participate in the interaction with the C-1 carbonyl group by water molecule-bridging hydrogen bonds during product **7** formation. To further elucidate the different structural basis of Fsa2 and Phm7 for their catalysis, we compared the modeled **6** in the active site of Phm7 with the complex structure of CghA with its product Sch210972 (PDB ID: 6KBC),[21] since Phm7 and CghA catalyze the same stereoselective cycloaddition reactions in phomasetin and Sch210972 biosynthesis.[18,25] The upper hydrophobic pocket of CghA contains similar residues to those in the upper hydrophobic pocket of Phm7 (Figure S10A). In the lower hydrophilic binding site, CghA contains the same Ser65 (corresponding to Ser69 in Phm7 and Gly67 in Fsa2) that forms a hydrogen bond with the lactam carbonyl group of Sch210972. These similarities lead to the similar binding styles of **6** and Sch210972 in the two active sites (Figures S10B and S10C). More hydrogen bonds can be observed between the terminal carboxyl group of Sch210972 with Asn364, Lys352, His94, and Asn82 in the lower hydrophilic binding site, further contributing to the substrate-binding orientation. Thus, based on the active site comparison and modeling experiments, the opposite substrate-binding orientations (differ by ∼180°) in Fsa2 and Phm7 may be attributed to the different hydrogen-bond interactions in their lower hydrophilic binding sites. The reverse catalytic stereoselectivities of Fsa2 and Phm7, as discussed above (Figure 4C,E), may be related to different shape complementarities of the diene/dienophile moieties to the active sites of Fsa2 and Phm7. The shape complementarities have been observed and mentioned in the ligand-binding complex structures of pericyclases LepI,[14] PhqE,[26] and PyrI4.[4] The molecular dynamics simulation experiments were further carried out for **5**-bound Fsa2 and Phm7 to investigate the shape complementarities. The molecular dynamics simulations show similar substrate-binding and shape complementarity results compared to those from the substrate modeling (Figures S11 and S12). Different side chain conformations of active site residues can be observed after molecular dynamics simulations, including new hydrogen bonds formed between the hydroxymethyl moiety of **5** and Tyr174 in Fsa2 (Figure S11A) or Trp345 in Phm7 (Figure S12A). The differences between molecular dynamics simulations and substrate modeling highlight the dynamic conformations of both substrate and active site residues in the binding process.

CONCLUSIONS

In summary, we solved the crystal structures of two pericyclases Fsa2 and Phm7 catalyzing [4 + 2] cycloadditions with reverse stereoselectivities in the biosynthesis of equisetin and phomasetin, which are two potent HIV-1 integrase inhibitors. The two crystal structures possess the "two-β barrel" folds and unusual active sites, enriching the structural diversity of this family of enzymes. Although the effort to solve complex structures of Fsa2 and Phm7 with product mimics failed, the differences of hydrophobic and hydrogen-bond interactions between Fsa2 and Phm7's active sites are clearly observed. Modeling of substrates and products into the active sites of Fsa2 and Phm7 and comparison with the complex structure of CghA with Sch210972 provide key structural information related to their catalytic stereoselectivities. The site-directed mutagenesis for Fsa2 and Phm7 and rational engineering of the two pericyclases to change their substrate promiscuities and catalytic stereoselectivities will be expected

https://doi.org/10.1021/acsomega.1c01593
ACS Omega 2021, 6, 12913−12922

in future experiments. As mentioned previously, the *in vitro* reaction system may not be a feasible system for mutagenesis and engineering due to purification and stability issues of synthesized substrate mimics. Thus, mutagenesis and engineering of *fsa2* or *phm7* in native producers or heterologous expression systems are promising in the generation of anti-HIV equisetin/phomasetin derivatives in the future.

MATERIALS AND METHODS

General Procedures. The genes *fsa2* (GenBank accession no. LC025956) and *phm7* (GenBank accession no. LC361337) were optimized for expression in *E. coli*, synthesized, and then individually cloned into the pET28b(+) vector. *E. coli* BL21 (DE3) (Beijing TransGen Biotech, Beijing, China) was used for protein overproduction. Plasmids used in our research are listed in Table S1. Fermentations were carried out in MQD-B1R shakers (Minquan Instrument Co., Ltd., Shanghai, China).

Gene Cloning and Plasmid Construction. The codon-optimized genes of *fsa2* and *phm7* were synthesized by Shanghai Langjin Biotech (LOGENBIO), then, *fsa2* was inserted into a pET28b(+) vector (Novagen) between the *Nde*I and *Hind*III sites to construct the plasmid pMM4005, and *phm7* was inserted into a pET28b(+) vector between the *Nde*I and *Xho*I sites to construct the plasmid pMM4006. The resulting plasmids pMM4005 and pMM4006 were confirmed by sequencing at Beijing RuiBioTech.

Protein Purification for Fsa2 and Phm7. *Selenomethionine-Labeled Fsa2 (Se-Fsa2).* For gene expression, the recombinant plasmid pMM4005 were transferred into *E. coli* BL21 (DE3) in lysogeny broth (LB) medium containing 60 μg/mL kanamycin for preculture inoculation for 10 h at 37 °C, 250 rpm. Then, 10 mL of seed culture obtained above was inoculated into 1 L of LB with 60 μg/mL kanamycin and incubated at 37 °C, 230 rpm until an OD_{600} of 1.0 was reached. The cells were harvested by centrifugation for 10 min at 4 °C, 4000 rpm, and washed mildly with 60 mL of medium A (17.1 g $Na_2HPO_4{\cdot}12H_2O$, 3 g KH_2PO_4, 0.5 g NaCl, 1 g NH_4Cl, 4 g glucose, 120 mg $MgSO_4$, 33 mg $CaCl_2$, 1 μg biotin, 1 μg thiamin, and 60 mg kanamycin in 1 L of dd H_2O). After centrifugation again, the cells were resuspended to 1 L of medium A, and fermentation was continued at 37 °C and 230 rpm until an OD_{600} of 1.5 was reached. Then, the culture was cooled down to 16 °C, 50 mg of selenomethionine and 0.5 mL of 500 mM isopropylthio-β-D-galactoside (IPTG) were added, and incubation was continued for another 20 h. The cells were harvested by centrifugation for 10 min at 4 °C, 4000 rpm, resuspended in 30 mL of lysis buffer (100 mM Tris, 15 mM imidazole, 300 mM NaCl, and 10% glycerol, pH 8.0), and lysed on ice by sonication. The lysate was clarified by centrifugation at 13,000 rpm for 60 min, and the supernatant containing Se-Fsa2 was loaded onto a 5 mL Histrap HP column (GE Healthcare Life Sciences) with the ÄKTA FPLC system (GE Healthcare Life Sciences). The Histrap HP column was eluted with two column volumes of buffer A (50 mM Tris, 20 mM imidazole, and 300 mM NaCl, pH 8.0), and Se-Fsa2 proteins were eluted with two column volumes of buffer B (50 mM Tris, 110 mM imidazole, and 300 mM NaCl, pH 8.0). Se-Fsa2 proteins were digested with thrombin for 12 h at 4 °C to remove the N-terminal His_6-tag. A second Histrap HP column was used to purify the Se-Fsa2 proteins without His_6-tag (in the flow-through part). The Se-Fsa2 proteins were exchanged to buffer C (20 mM Tris and 10 mM NaCl, pH 8.0) using a PD10 column (GE Healthcare Life Sciences) and loaded onto an anion-exchange Resource Q column (GE Healthcare Life Sciences), which was eluted with an increased gradient of buffer D (20 mM Tris and 1 M NaCl, pH 8.0) in buffer C. The Se-Fsa2 proteins were further purified with a size exclusion column (Superdex 200 Increase 10/300 GL, GE Healthcare Life Sciences) eluted with buffer E (20 mM TEAOH, 20 mM NaCl, and 10 mM KCl, pH 7.5). Purified proteins were analyzed by SDS−PAGE and concentrated with an Amicon Ultra-15 concentrator (Millipore) for crystallization.

Fsa2. The recombinant plasmid pMM4005 was transferred into *E. coli* BL21 (DE3) in LB medium containing 60 μg/mL kanamycin for preculture inoculation for 10 h at 37 °C, 250 rpm. Then, 10 mL of seed culture obtained above was inoculated into 1 L of LB with 60 μg/mL kanamycin and incubated at 37 °C, 230 rpm until an OD_{600} of 0.8 was reached. Then, expression of *fsa2* was induced by IPTG with a final concentration of 0.25 mM at 16 °C for 20 h. The cells were harvested by centrifugation for 15 min at 4 °C, 4000 rpm and resuspended in 30 mL of lysis buffer (100 mM Tris, 15 mM imidazole, 300 mM NaCl, and 10% glycerol, pH 8.0). The protein was purified using a Histrap HP column, digested by thrombin to remove the His_6-tag, purified using a Histrap HP column, anion exchanger Q HP column, and size exclusion column according to the procedures described above. Purified proteins were analyzed by SDS−PAGE and then concentrated with an Amicon Ultra-15 concentrator for crystallization.

Phm7. The purification of Phm7 by transformation of pMM4006 into *E. coli* BL21 (DE3) was carried out according to the similar procedures as those for Fsa2. Purified proteins were analyzed by SDS−PAGE and then concentrated with an Amicon Ultra-15 concentrator for crystallization.

Crystallization, X-ray Fraction Data Collection, and Structural Elucidation. Initial crystallization screening of Fsa2 was performed at 16 °C in 24-well plates with the hanging-drop vapor-diffusion method, and crystals were observed in a screening kit Index-47 (Hampton Research). The crystals of Se-Fsa2 were obtained by mixing 2 μL of protein solution (4 mg/mL in 20 mM TEAOH, 20 mM NaCl, and 10 mM KCl, pH 7.5) and 2 μL of reservoir (0.1 M Bis-Tris and 28% PEG 2000 MME, pH 6.5) after 14 days at 16 °C. However, the crystals gave weak diffraction. Great effort was made for quality improvement of the crystals by optimizing protein concentrations, PEG 2000 MME concentrations, pH values, and temperatures. High-quality crystals of Se-Fsa2 (final concentration: 2 mg/mL) were obtained in 0.05 M Bis-Tris and 14% PEG 2000 MME, pH 6.3 at 4 °C after 3 months. Se-Fsa2 crystals were flash-freezed with a cryoprotectant (crystallization buffer containing 30% glycerol) and stored in liquid nitrogen for data collection.

The crystallization screening of Phm7 was performed with the sitting-drop vapor-diffusion method with a robot (Mosquito LCP, LBD Life sciences TTP, China) at 16 °C, and crystals of Phm7 were observed in a screening kit SaltRx1-35 (Hampton Research). Crystallization optimization was performed with the hanging-drop vapor-diffusion method using 24-well plates. High-quality crystals of Phm7 (final concentration: 12 mg/mL) were obtained in 0.05 M Bis-Tris propane and 0.68 M sodium malonate, pH 7.0 at 16 °C after 7 days. Phm7 crystals were flash-freezed with a cryoprotectant (crystallization buffer containing 30% glycerol) and stored in liquid nitrogen for data collection.

https://doi.org/10.1021/acsomega.1c01593
ACS Omega 2021, 6, 12913−12922

The X-ray diffraction data of Se-Fsa2 were collected at beamline BL17U1 at the Shanghai Synchrotron Radiation Facility (SSRF)[20] with a wavelength of 0.97913 Å. The diffraction data were processed and scaled with HKL-3000.[27] The Se-SAD phase was determined and a partial structural model of Se-Fsa2 was traced in PHENIX.AutoSol.[28] The structural of Se-Fsa2 was initially built with PHENIX.AutoBuild and then built manually with Coot[29] and then refined with PHENIX.refine[30] and Refmac5.[31] The structure of Se-Fsa2 was solved at 2.46 Å by SAD and the resolution was improved to 2.00 Å by molecular replacement using another set of Se-Fsa2 diffraction data that was collected with an XtaLAB Synergy diffractometer system (1.54056 Å).

The X-ray diffraction data of Phm7 were collected with an XtaLAB Synergy diffractometer system (1.54056 Å). The data were processed and scaled using *CrysAlis*^{Pro} software.[32] The crystal structure of Phm7 was solved by molecular replacement using Se-Fsa2 as the searching model. Both Se-Fsa2 and Phm7 structures were checked using the program MolProbity[33] and PROCHECK.[34] Relevant statistics are summarized in Table S2.

Docking Experiments. The docking experiments were performed using AutoDock 4.2.27.[35] Before the docking, water molecules were removed from Fsa2 and Phm7. AutoDockTools 1.5.6 was used to prepare the substrate and products **5**−**7** and macromolecules Fsa2 and Phm7. The default parameters were used to set the torsion constraints for **5**−**7**, and charges and hydrogen atoms were added to Fsa2 and Phm7 proteins. The structures of Fsa2 and Phm7 were superposed with each other for preparing the grid box. A grid box of 20 × 40 × 16 nm^3 ($x \times y \times z$) with the search space center of x = −36.33, y = −9.91, and z = −10.58 was created (grid spacing: 0.375 Å, smoothing: 0.5 Å). All docking experiments were performed using a Lamarkian Genetic Algorithm. The independent flexible docking runs were set as 400, and other search parameters were used with default values. For the modeling of substrate **5**, the modeling hit with the lowest binding energy among those with terminal-conjugated $\Delta^{3,4}$ and $\Delta^{5,6}$- diene moiety close to the $\Delta^{2,11}$ dienophile moiety was selected for substrate-binding analysis. For the modeling of products **6** and **7**, the modeling hits with the lowest binding energy among those possessing similar orientations to modeled **5** in Fsa2 or Phm7 were used for product-binding analysis.

Molecular Dynamics Simulation. The simulation was performed with the AMBER 14 molecular simulation package.[36] To obtain molecular mechanical parameters for modified residues, ab initio quantum chemical methods were employed using the Gaussian 09 program.[37] The geometry was fully optimized, and then, the electrostatic potentials around them were determined at the B3LYP/6-31G* level of theory. The RESP strategy was used to obtain the partial atomic charges.

The starting **5**-bound structures from the substrate modeling were solvated in TIP3P water using an octahedral box, which extended 8 Å away from any solute atom. To neutralize the negative charges of simulated molecules, Na^+ counterions were placed next to each phosphate group. Molecular dynamics simulation was carried out using the PMEMD module of AMBER 14. The calculations began with 500 steps of steepest descent followed by 500 steps of conjugate gradient minimization with a large constraint of 500 kcal mol^{-1} Å^{-2} on the atoms of the Fsa2 and Phm7. Then, 1000 steps of steepest descent followed by 1500 steps of conjugate gradient minimization with no restraint on the complex atoms were performed. Subsequently, after 20 ps of molecular dynamics, during which the temperature was slowly increased from 0 to 300 K with weak (10 kcal mol^{-1} Å^{-2}) restraint on the Fsa2 and Phm7, the final unrestrained production simulations of 20.0 ns were carried out at constant pressure (1 atm) and temperature (300 K). In the entire simulation, SHAKE was applied to all hydrogen atoms. Periodic boundary conditions with minimum image conventions were applied to calculate the nonbonded interactions. A cutoff of 10 Å was used for the Lennard-Jones interactions. The final conformations of the complexes were produced from the 1000 steps of the minimized averaged structure of the last 8.0 ns of molecular dynamics.

■ ASSOCIATED CONTENT

Supporting Information

The Supporting Information is available free of charge at https://pubs.acs.org/doi/10.1021/acsomega.1c01593.

X-ray diffraction data collection and structural refinement statistics, summary of biosynthetic pericyclases, and figures related to the analyses of Fsa2 and Phm7 structures (PDF)

■ AUTHOR INFORMATION

Corresponding Author

Ming Ma − *State Key Laboratory of Natural and Biomimetic Drugs, School of Pharmaceutical Sciences, Peking University, Beijing 100191, China;* orcid.org/0000-0001-8311-3892; Email: mma@bjmu.edu.cn

Authors

Changbiao Chi − *State Key Laboratory of Natural and Biomimetic Drugs, School of Pharmaceutical Sciences, Peking University, Beijing 100191, China*

Zhengdong Wang − *State Key Laboratory of Natural and Biomimetic Drugs, School of Pharmaceutical Sciences, Peking University, Beijing 100191, China*

Tan Liu − *State Key Laboratory of Natural and Biomimetic Drugs, School of Pharmaceutical Sciences, Peking University, Beijing 100191, China*

Zhongyi Zhang − *State Key Laboratory of Natural and Biomimetic Drugs, School of Pharmaceutical Sciences, Peking University, Beijing 100191, China*

Huan Zhou − *Shanghai Synchrotron Radiation Facility, Shanghai Advanced Research Institute, Chinese Academy of Sciences, Shanghai 201204, China*

Annan Li − *State Key Laboratory of Natural and Biomimetic Drugs, School of Pharmaceutical Sciences, Peking University, Beijing 100191, China*

Hongwei Jin − *State Key Laboratory of Natural and Biomimetic Drugs, School of Pharmaceutical Sciences, Peking University, Beijing 100191, China*

Hongli Jia − *State Key Laboratory of Natural and Biomimetic Drugs, School of Pharmaceutical Sciences, Peking University, Beijing 100191, China*

Fuling Yin − *State Key Laboratory of Natural and Biomimetic Drugs, School of Pharmaceutical Sciences, Peking University, Beijing 100191, China*

Donghui Yang − *State Key Laboratory of Natural and Biomimetic Drugs, School of Pharmaceutical Sciences, Peking University, Beijing 100191, China*

Complete contact information is available at:

https://doi.org/10.1021/acsomega.1c01593
ACS Omega 2021, 6, 12913−12922

https://pubs.acs.org/10.1021/acsomega.1c01593

Author Contributions

§C.C. and Z.W. contributed equally.

Notes

The authors declare no competing financial interest.

■ ACKNOWLEDGMENTS

This research was supported in part by the National Key Research and Development Program of China (2019YFC0312502), the National Natural Science Foundation of China (grant numbers 21877002, 81673332, 81991525, and 22077007), the key project at the central government level: the ability establishment of sustainable use for valuable Chinese medicine resources (2060302-1903-03), and the China Postdoctoral Science Foundation (2019M660362).

■ REFERENCES

(1) Jamieson, C. S.; Ohashi, M.; Liu, F.; Tang, Y.; Houk, K. N. The Expanding World of Biosynthetic Pericyclases: Cooperation of Experiment and Theory for Discovery. *Nat. Prod. Rep.* **2019**, *36*, 698−713.

(2) Jeon, B.-S.; Wang, S.-A.; Ruszczycky, M. W.; Liu, H.-W. Natural [4 + 2]-Cyclases. *Chem. Rev.* **2017**, *117*, 5367−5388.

(3) Kim, H. J.; Ruszczycky, M. W.; Choi, S.-H.; Liu, Y.-N.; Liu, H.-W. Enzyme-Catalysed [4 + 2] Cycloaddition Is a Key Step in the Biosynthesis of Spinosyn A. *Nature* **2011**, *473*, 109−112.

(4) Zheng, Q.; Guo, Y.; Yang, L.; Zhao, Z.; Wu, Z.; Zhang, H.; Liu, J.; Cheng, X.; Wu, J.; Yang, H.; Jiang, H.; Pan, L.; Liu, W. Enzyme-Dependent [4 + 2] Cycloaddition Depends on Lid-like Interaction of the N-Terminal Sequence with the Catalytic Core in PyrI4. *Cell Chem. Biol.* **2016**, *23*, 352−360.

(5) Zheng, Q.; Gong, Y.; Guo, Y.; Zhao, Z.; Wu, Z.; Zhou, Z.; Chen, D.; Pan, L.; Liu, W. Structural Insights into a Flavin-Dependent [4 + 2] Cyclase that Catalyzes trans-Decalin Formation in Pyrroindomycin Biosynthesis. *Cell Chem. Biol.* **2018**, *25*, 718−727.

(6) Li, L.; Yu, P.; Tang, M.-C.; Zou, Y.; Gao, S.-S.; Hung, Y.-S.; Zhao, M.; Watanabe, K.; Houk, K. N.; Tang, Y. Biochemical Characterization of a Eukaryotic Decalin-Forming Diels-Alderase. *J. Am. Chem. Soc.* **2016**, *138*, 15837−15840.

(7) Byrne, M. J.; Lees, N. R.; Han, L.-C.; Van Der Kamp, M. W.; Mulholland, A. J.; Stach, J. E. M.; Willis, C. L.; Race, P. R. The Catalytic Mechanism of a Natural Diels-Alderase Revealed in Molecular Detail. *J. Am. Chem. Soc.* **2016**, *138*, 6095−6098.

(8) Li, Q.; Ding, W.; Tu, J.; Chi, C.; Huang, H.; Ji, X.; Yao, Z.; Ma, M.; Ju, J. Nonspecific Heme-Binding Cyclase, AbmU, Catalyzes [4 + 2] Cycloaddition during Neoabyssomicin Biosynthesis. *ACS Omega* **2020**, *5*, 20548−20557.

(9) Bogart, J. W.; Bowers, A. A. Thiopeptide Pyridine Synthase TbtD Catalyzes an Intermolecular Formal Aza-Diels-Alder Reaction. *J. Am. Chem. Soc.* **2019**, *141*, 1842−1846.

(10) Wever, W. J.; Bogart, J. W.; Baccile, J. A.; Chan, A. N.; Schroeder, F. C.; Bowers, A. A. Chemoenzymatic Synthesis of Thiazolyl Peptide Natural Products Featuring an Enzyme-Catalyzed Formal [4 + 2] Cycloaddition. *J. Am. Chem. Soc.* **2015**, *137*, 3494−3497.

(11) Cogan, D. P.; Hudson, G. A.; Zhang, Z.; Pogorelov, T. V.; Van Der Donk, W. A.; Mitchell, D. A.; Nair, S. K. Structural Insights into Enzymatic [4 + 2] Aza-Cycloaddition in Thiopeptide Antibiotic Biosynthesis. *Proc. Natl. Acad. Sci. U.S.A.* **2017**, *114*, 12928−12933.

(12) Zhang, B.; Wang, K.-B.; Wang, W.; Wang, X.; Liu, F.; Zhu, J.; Shi, J.; Li, L.-Y.; Han, H.; Xu, K.; Qiao, H.-Y.; Zhang, X.; Jiao, R.-H.; Houk, K. N.; Liang, Y.; Tan, R.-X.; Ge, H.-M. Enzyme-Catalysed [6 + 4] Cycloadditions in the Biosynthesis of Natural Products. *Nature* **2019**, *568*, 122−126.

(13) Gao, L.; Su, C.; Du, X.; Wang, R.; Chen, S.; Zhou, Y.; Liu, C.; Liu, X.; Tian, R.; Zhang, L.; Xie, K.; Chen, S.; Guo, Q.; Guo, L.; Hano, Y.; Shimazaki, M.; Minami, A.; Oikawa, H.; Huang, N.; Houk, K. N.; Huang, L.; Dai, J.; Lei, X. FAD-Dependent Enzyme-Catalysed Intermolecular [4 + 2] Cycloaddition in Natural Product Biosynthesis. *Nat. Chem.* **2020**, *12*, 620−628.

(14) Cai, Y.; Hai, Y.; Ohashi, M.; Jamieson, C. S.; Garcia-Borras, M.; Houk, K. N.; Zhou, J.; Tang, Y. Structural Basis for Stereoselective Dehydration and Hydrogen-Bonding Catalysis by the SAM-Dependent Pericyclase LepI. *Nat. Chem.* **2019**, *11*, 812−820.

(15) Ohashi, M.; Liu, F.; Hai, Y.; Chen, M.; Tang, M.-C.; Yang, Z.; Sato, M.; Watanabe, K.; Houk, K. N.; Tang, Y. SAM-Dependent Enzyme-Catalysed Pericyclic Reactions in Natural Product Biosynthesis. *Nature* **2017**, *549*, 502−506.

(16) Ohashi, M.; Jamieson, C. S.; Cai, Y.; Tan, D.; Kanayama, D.; Tang, M.-C.; Anthony, S. M.; Chari, J. V.; Barber, J. S.; Picazo, E.; Kakule, T. B.; Cao, S.; Garg, N. K.; Zhou, J.; Houk, K. N.; Tang, Y. An Enzymatic Alder-Ene Reaction. *Nature* **2020**, *586*, 64−69.

(17) Kato, N.; Nogawa, T.; Hirota, H.; Jang, J.-H.; Takahashi, S.; Ahn, J. S.; Osada, H. A New Enzyme Involved in the Control of the Stereochemistry in the Decalin Formation during Equisetin Biosynthesis. *Biochem. Biophys. Res. Commun.* **2015**, *460*, 210−215.

(18) Kato, N.; Nogawa, T.; Takita, R.; Kinugasa, K.; Kanai, M.; Uchiyama, M.; Osada, H.; Takahashi, S. Control of the Stereochemical Course of [4+2] Cycloaddition during trans -Decalin Formation by Fsa2-Family Enzymes. *Angew. Chem., Int. Ed.* **2018**, *57*, 9754−9758.

(19) Singh, S. B.; Zink, D. L.; Goetz, M. A.; Dombrowski, A. W.; Polishook, J. D.; Hazuda, D. J. Equisetin and a Novel Opposite Stereochemical Homolog Phomasetin, Two Fungal Metabolites as Inhibitors of HIV-1 Integrase. *Tetrahedron Lett.* **1998**, *39*, 2243−2246.

(20) Wang, Q.-S.; Zhang, K.-H.; Cui, Y.; Wang, Z.-J.; Pan, Q.-Y.; Liu, K.; Sun, B.; Zhou, H.; Li, M.-J.; Xu, Q.; Xu, C.-Y.; Yu, F.; He, J.-H. Upgrade of Macromolecular Crystallography Beamline BL17U1 at SSRF. *Nucl. Sci. Tech.* **2018**, *29*, 68.

(21) Sato, M.; Kishimoto, S.; Yokoyama, M.; Jamieson, C. S.; Narita, K.; Maeda, N.; Hara, K.; Hashimoto, H.; Tsunematsu, Y.; Houk, K. N.; Tang, Y.; Watanabe, K. Catalytic mechanism and endo-to-exo selectivity reversion of an octalin-forming natural Diels-Alderase. *Nat. Catal.* **2021**, *4*, 223−232.

(22) Chiu, H.-J.; Bakolitsa, C.; Skerra, A.; Lomize, A.; Carlton, D.; Miller, M. D.; Krishna, S. S.; Abdubek, P.; Astakhova, T.; Axelrod, H. L.; Clayton, T.; Deller, M. C.; Duan, L.; Feuerhelm, J.; Grant, J. C.; Grzechnik, S. K.; Han, G. W.; Jaroszewski, L.; Jin, K.-K.; Klock, H. E.; Knuth, M. W.; Kozbial, P.; Kumar, A.; Marciano, D.; McMullan, D.; Morse, A. T.; Nigoghossian, E.; Okach, L.; Paulsen, J.; Reyes, R.; Rife, C. L.; Van Den Bedem, H.; Weekes, D.; Xu, Q.; Hodgson, K. O.; Wooley, J.; Elsliger, M.-A.; Deacon, A. M.; Godzik, A.; Lesley, S. A.; Wilson, I. A. Structure of the First Representative of Pfam Family PF09410 (DUF2006) Reveals a Structural Signature of the Calycin Superfamily That Suggests a Role in Lipid Metabolism. *Acta Crystallogr., Sect. F: Struct. Biol. Cryst. Commun.* **2010**, *66*, 1153−1159.

(23) Li, X.; Zheng, Q.; Yin, J.; Liu, W.; Gao, S. Chemo-Enzymatic Synthesis of Equisetin. *Chem. Commun.* **2017**, *53*, 4695−4697.

(24) Yin, J.; Kong, L.; Wang, C.; Shi, Y.; Cai, S.; Gao, S. Biomimetic Synthesis of Equisetin and (+)-Fusarisetin A. *Isr. J. Chem.* **2013**, *19*, 13040−13046.

(25) Sato, M.; Yagishita, F.; Mino, T.; Uchiyama, N.; Patel, A.; Chooi, Y.-H.; Goda, Y.; Xu, W.; Noguchi, H.; Yamamoto, T.; Hotta, K.; Houk, K. N.; Tang, Y.; Watanabe, K. Involvement of Lipocalin-like CghA in Decalin-Forming Stereoselective Intramolecular [4+2] Cycloaddition. *ChemBioChem* **2015**, *16*, 2294−2298.

(26) Dan, Q.; Newmister, S. A.; Klas, K. R.; Fraley, A. E.; McAfoos, T. J.; Somoza, A. D.; Sunderhaus, J. D.; Ye, Y.; Shende, V. V.; Yu, F.; Sanders, J. N.; Brown, W. C.; Zhao, L.; Paton, R. S.; Houk, K. N.; Smith, J. L.; Sherman, D. H.; Williams, R. M. Fungal Indole Alkaloid Biogenesis Through Evolution of a Bifunctional Reductase/Diels-Alderase. *Nat. Chem.* **2019**, *11*, 972−980.

(27) Minor, W.; Cymborowski, M.; Otwinowski, Z.; Chruszcz, M. HKL-3000: The Integration of Data Reduction and Structure

Solution - From Diffraction Images to an Initial Model in Minutes. *Acta Crystallogr., Sect. D: Biol. Crystallogr.* **2006**, *62*, 859−866.
(28) Terwilliger, T. C.; Adams, P. D.; Read, R. J.; McCoy, A. J.; Moriarty, N. W.; Grosse-Kunstleve, R. W.; Afonine, P. V.; Zwart, P. H.; Hung, L.-W. Decision-making in structure solution using Bayesian estimates of map quality: the PHENIX AutoSolwizard. *Acta Crystallogr., Sect. D: Biol. Crystallogr.* **2009**, *65*, 582−601.
(29) Emsley, P.; Cowtan, K. Coot: Model-Building Tools for Molecular Graphics. *Acta Crystallogr., Sect. D: Biol. Crystallogr.* **2004**, *60*, 2126−2132.
(30) Adams, P. D.; Afonine, P. V.; Bunkóczi, G.; Chen, V.-B.; Davis, I. W.; Echols, N.; Headd, J. J.; Hung, L.-W.; Kapral, G. J.; Grosse-Kunstleve, R. W.; McCoy, A. J.; Moriarty, N. W.; Oeffner, R.; Read, R. J.; Richardson, D. C.; Richardson, J. S.; Terwilliger, T. C.; Zwart, P. H. PHENIX: A Comprehensive Python-Based System for Macromolecular Structure Solution. *Acta Crystallogr., Sect. D: Biol. Crystallogr.* **2010**, *66*, 213−221.
(31) Murshudov, G. N.; Skubák, P.; Lebedev, A. A.; Pannu, N. S.; Steiner, R. A.; Nicholls, R. A.; Winn, M. D.; Long, F.; Vagin, A. A. REFMAC5 for the Refinement of Macromolecular Crystal Structures. *Acta Crystallogr., Sect. D: Biol. Crystallogr.* **2011**, *67*, 355−367.
(32) Rothkirch, A.; Gatta, G. D.; Meyer, M.; Merkel, S.; Merlini, M.; Liermann, H.-P. Single-Crystal Diffraction at the Extreme Conditions Beamline P02.2: Procedure for Collecting and Analyzing High-Pressure Single-Crystal Data. *J. Synchrotron Radiat.* **2013**, *20*, 711−720.
(33) Davis, I. W.; Leaver-Fay, A.; Chen, V.-B.; Block, J. N.; Kapral, G. J.; Wang, X.; Murray, L. W.; Arendall, W. B.; Snoeyink, J.; Richardson, J. S.; Richardson, D. C. MolProbity: All-Atom Contacts and Structure Validation for Proteins and Nucleic Acids. *Nucleic Acids Res.* **2007**, *35*, 375−383.
(34) Laskowski, R. A.; MacArthur, M. W.; Moss, D. S.; Thornton, J. M. PROCHECK: A Program to Check the Stereochemical Quality of Protein Structures. *J. Appl. Crystallogr.* **1993**, *26*, 283−291.
(35) Morris, G. M.; Huey, R.; Lindstrom, W.; Sanner, M. F.; Belew, R. K.; Goodsell, D. S.; Olson, A. J.; AutoDockTools4. AutoDock4 and AutoDockTools4: Automated docking with selective receptor flexibility. *J. Comput. Chem.* **2009**, *30*, 2785−2791.
(36) Case, D. A.; Darden, T. A.; Cheatham, T. E.; Simmerling, C. L.; Wang, J.; Duke, R. E.; Luo, R.; Walker, R. C.; Zhang, W.; Merz, K. M.; Roberts, B.; Wang, B.; Hayik, S.; Roitberg, A.; Seabra, G.; Kolossváry, I.; Wong, K. F.; Paesani, F.; Vanicek, J.; Liu, J.; Wu, X.; Brozell, S. R.; Steinbrecher, T.; Gohlke, H.; Cai, Q.; Ye, X.; Wang, J.; Hsieh, M.-J.; Cui, G.; Roe, D. R.; Mathews, D. H.; Seetin, M. G.; Sagui, C.; Babin, V.; Luchko, T.; Gusarov, S.; Kovalenko, A.; Kollman, P. A. *Amber14*, version AMBER14; University of California: San Francisco, 2014.
(37) Frisch, M. J.; Trucks, G. W.; Schlegel, H. B.; Scuseria, G. E.; Robb, M. A.; Cheeseman, J. R.; Scalmani, G.; Barone, V.; Mennucci, B.; Petersson, G. A.; Nakatsuji, H.; Caricato, M.; Li, X.; Hratchian, H. P.; Izmaylov, A. F.; Bloino, J.; Zheng, G.; Sonnenberg, J. L.; Hada, M.; Ehara, M.; Toyota, K.; Fukuda, R.; Hasegawa, J.; Ishida, M.; Nakajima, T.; Honda, Y.; Kitao, O.; Nakai, H.; Vreven, T.; Montgomery, J. A.; Peralta, J. E.; Ogliaro, F.; Bearpark, M.; Heyd, J. J.; Brothers, E.; Kudin, K. N.; Staroverov, V. N.; Kobayashi, R.; Normand, J.; Raghavachari, K.; Rendell, A.; Burant, J. C.; Iyengar, S. S.; Tomasi, J.; Cossi, M.; Rega, N.; Millam, J. M.; Klene, M.; Knox, J. E.; Cross, J. B.; Bakken, V.; Adamo, C.; Jaramillo, J.; Gomperts, R.; Stratmann, R. E.; Yazyev, O.; Austin, A. J.; Cammi, R.; Pomelli, C.; Ochterski, J. W.; Martin, R. L.; Morokuma, K.; Zakrzewski, V. G.; Voth, G. A.; Salvador, P.; Dannenberg, J. J.; Dapprich, S.; Daniels, A. D.; Farkas, O.; Foresman, J. B.; Ortiz, J. V.; Cioslowski, J.; Fox, D. J. *Gaussian 16*, Revision B.01; Gaussian Inc: Wallingford CT, 2016.

https://doi.org/10.1021/acsomega.1c01593
ACS Omega 2021, 6, 12913−12922